**nature biotechnology**

# Multiplexed mass cytometry profiling of cellular states perturbed by small-molecule regulators

Bernd Bodenmiller[1,5,6], Eli R Zunder[1,6], Rachel Finck[1,6], Tiffany J Chen[1–3], Erica S Savig[1,4], Robert V Bruggner[1,2], Erin F Simonds[1], Sean C Bendall[1], Karen Sachs[1], Peter O Krutzik[1] & Garry P Nolan[1]

**Mass cytometry facilitates high-dimensional, quantitative analysis of the effects of bioactive molecules on human samples at single-cell resolution, but instruments process only one sample at a time. Here we describe mass-tag cellular barcoding (MCB), which increases mass cytometry throughput by using $n$ metal ion tags to multiplex up to $2^n$ samples. We used seven tags to multiplex an entire 96-well plate, and applied MCB to characterize human peripheral blood mononuclear cell (PBMC) signaling dynamics and cell-to-cell communication, signaling variability between PBMCs from eight human donors, and the effects of 27 inhibitors on this system. For each inhibitor, we measured 14 phosphorylation sites in 14 PBMC types at 96 conditions, resulting in 18,816 quantified phosphorylation levels from each multiplexed sample. This high-dimensional, systems-level inquiry allowed analysis across cell-type and signaling space, reclassified inhibitors and revealed off-target effects. High-content, high-throughput screening with MCB should be useful for drug discovery, preclinical testing and mechanistic investigation of human disease.**

High-throughput *in vitro* screening has accelerated the discovery of drug candidates, but paradoxically coincides with a steep decline in the approval rate for novel molecular entities[1,2]. The enormous rate of attrition as drug candidates move through clinical development can be partly attributed to the disconnect between human physiology and the *in vitro* screening regimen, which cannot measure efficacy in heterogeneous tissues or detect off-target toxicities[2–4]. If the original screening regimen more closely reflected human physiology by using human samples, such as PBMCs or cancer biopsies, efficacy and toxicity could be identified earlier in the development process. High-dimensional analysis of cellular signaling networks can provide a detailed representation of cellular state[5,6]; it is often presumed that additional biologically informative measurements of markers of pathways would be a desirable outcome for high-throughput screening. Compounds that target certain signaling molecules can lead to successful therapeutic outcomes[7], but many compounds that target known oncogenic lesions lack clinical efficacy[8]. As such, the *in vitro* targets of a drug candidate cannot be used to accurately predict efficacy *in vivo* owing to signaling network complexity and differences between patients or cell subpopulations of the same patient[6,7,9–12]. Therefore, high-content, single-cell analysis of signaling networks in human samples during drug development could provide welcome insight into the manifold effects of drugs on cellular systems.

We propose that an ideal drug-screening approach should, first, be based on primary human samples, with systemic behavior that resembles normal physiology and the targeted disease state. Second, subpopulation-specific, system-wide signaling networks and their correlation to cell and disease phenotypes should be quantified,

providing a comprehensive view of the cellular state. Third, intercellular communication and emergent systems properties should be evaluated. And, lastly, measurements should be performed with high throughput. A screening approach with these features would enable the identification of compounds with *in vivo* efficacy against the targeted disease and low toxicity at the earliest stage of drug discovery.

Some methods have attempted to implement these features. Parallel enzymatic or phage display assays offer exceptional *in vitro* selectivity profiling[13–17], but do not provide *in vivo* data. Cellular assays based on proliferation, apoptosis or expression of reporter proteins approximate *in vivo* activity[18], but drug selectivity, mechanism of action and signaling network responses cannot be determined. Gene expression analysis[19,20] and liquid chromatography coupled to tandem mass spectrometry[6,21,22] measure thousands of parameters, but lack high throughput and single-cell resolution[23,24]. High-throughput microscopy offers deep characterization of single cells[23–25], but the limited number of surface and signaling molecules measured simultaneously restricts the breadth of analysis.

Fluorescence-based flow cytometry (FBFC) permits measurement of up to 12 molecules on a single cell simultaneously[26–28], allowing cell subpopulations and their signaling network states to be determined at the same time[29]. Drug-screening applications for FBFC have been implemented by hardware[30,31] or by sample multiplexing with fluorescent cell barcoding (FCB)[32,33]. With these adaptations, FBFC has become a powerful tool for drug screening and preclinical analysis. FBFC falls short of the ideal drug screening method, however, because the number of simultaneously measured parameters is limited owing to spectral overlap[27], hampering the comprehensive

[1]Baxter Laboratory in Stem Cell Biology, Department of Microbiology and Immunology, Stanford University, Stanford, California, USA. [2]Biomedical Informatics Program, Stanford University, Stanford, California, USA. [3]Department of Computer Science, Stanford University, Stanford, California, USA. [4]Cancer Biology Program, Stanford University, Stanford, California, USA. [5]Present address: Institute of Molecular Life Sciences, University of Zurich, Zurich, Switzerland. [6]These authors contributed equally to this work. Correspondence should be addressed to G.P.N. (gnolan@stanford.edu).

**Figure 1** Mass-tag cell barcoding. (**a**) Cells were covalently labeled with a bifunctional compound, maleimido-mono-amide-DOTA (mDOTA). This compound can be loaded with a lanthanide(III) isotope ion, and reacts covalently with cellular thiol groups through the maleimide moiety. (**b**) Seven unique lanthanide isotopes were used to generate 128 combinations, enough to barcode each sample in a 96-well plate are shown. The seven lanthanide isotopes, their masses and their locations on the 96-well plate are shown. (**c**) A density dot plot of barcoded cells is shown with the *y*-axis and *x*-axis plot showing barcoding (BC) channel 1 (lanthanum 139) versus barcoding channel 2 (praseodymium 141). Cells positive and negative for a given channel are indicated. (**d**) K562 cells were stimulated with orthovanadate, placed in a 96-well plate as geometrical patterns (checkerboard or striped pattern), barcoded, analyzed by mass cytometry and subsequently deconvoluted using Boolean gating to validate the accuracy of the de-barcoding. The two resulting heatmaps of the measured SLP76-Tyr696 phosphorylation levels are shown.

analysis of signaling network states within complex cell populations.

A recent advance in flow cytometry—mass cytometry—increases the number of parameters that can be measured, reduces overlap between measurement channels and eliminates background autofluorescence[34,35]. For mass cytometry, antibodies are labeled with isotopically pure metals[36] and quantified by inductively coupled plasma mass spectrometry. Current labeling techniques allow for 34 parameter measurements[35]. The large number of parallel measurements per cell makes mass cytometry an ideal method to assay drug candidates for cellular efficacy and selectivity.

To bring mass cytometry closer to the ideal screening approach, we have developed MCB, a cell-based multiplexing technique analogous to FCB, which improves sample throughput, reduces antibody consumption and ensures uniformity of the antibody stain across samples. In MCB, cells in each sample are tagged with a unique combination of mass tags before samples are combined. We arrayed samples in a 96-well format, which we then multiplexed and analyzed on one run through a mass cytometer. We used MCB to study PBMC signaling dynamics and cell-to-cell communication, to measure the variability of PBMC signaling responses between eight human donors and to define the effects of 27 kinase inhibitors on 14 PBMC subpopulations. In contrast to conventional approaches, which may use a single molecular readout of a signaling protein and pathway, we measured the concentration of 14 signaling proteins. This large number of simultaneously measured parameters enabled the context-specific classification of inhibitors and cell types. This analysis revealed that none of the compounds tested was specific for a single cell type, that inhibitor activity and selectivity were strongly dependent on context, and that the established topology of hierarchical relationships among PBMC cell types could be recapitulated based on signaling network responses alone.

## RESULTS
### Mass-tag cellular multiplexing
For mass cytometry the lanthanide series of transition metal elements is used as they are normally not present in biological samples, a large number of stable isotopes that can be enriched to high

purity are available, and their +3 oxidation state allows chelation into cell-labeling reagents. For MCB, we used the bifunctional molecule maleimido-mono-amide-DOTA (mDOTA) for chelation (**Fig. 1a**). The DOTA moiety chelates rare earth metal lanthanide(III) ions with a $K_d$ of $\sim 10^{-16}$ and the maleimide moiety rapidly reacts covalently with cellular thiol groups (**Fig. 1a** and **Supplementary Fig. 1**). Using binary combinations of seven preloaded mDOTA-lanthanide(III) reagents, 128 ($2^7$) combinations are possible, enabling all of the wells in a 96-well plate to be multiplexed in a single reaction (**Fig. 1b**). The MCB protocol is experimentally similar to the FCB protocol (**Supplementary Note 1**)[32,33], and after measurement, the data set is deconvolved with Boolean gating on the mDOTA-lanthanide(III) channels (**Fig. 1c**).

To test the accuracy and robustness of the MCB method, we used two reference cell samples differing in the abundance of phosphorylation on Tyr696 on the SH2 domain–containing 76-kDa leukocyte protein (SLP76) (**Supplementary Fig. 2**). We arranged the samples in checkerboard or striped patterns on 96-well plates for MCB analysis. After 96-well multiplexing, mass cytometry analysis of Tyr696 phosphorylation, and deconvolution, we were able to accurately recover the patterns (**Fig. 1d**). The resulting Z-prime values (a measure of the quality for an assay for high-throughput screening approaches) from the checkerboard and striped 96-well plates were 0.61 and 0.58, respectively, indicating that MCB is suitably robust for high-throughput drug screening applications.

### Time-course analysis of PBMC signaling
To confirm that MCB allows detection of physiological signaling events in PBMCs and to assess subpopulation-specific signaling dynamics, we used MCB (**Supplementary Fig. 3**) to carry out a 96-sample time-course experiment from 0 to 4 h (**Fig. 2a** and **Supplementary Results 1**). Fourteen signaling nodes and 10 cell-surface markers were measured over 12 stimulation conditions from one donor sample (**Fig. 2a,b**). To identify PBMC populations (**Fig. 2c**) and their signaling response, we applied spanning-tree
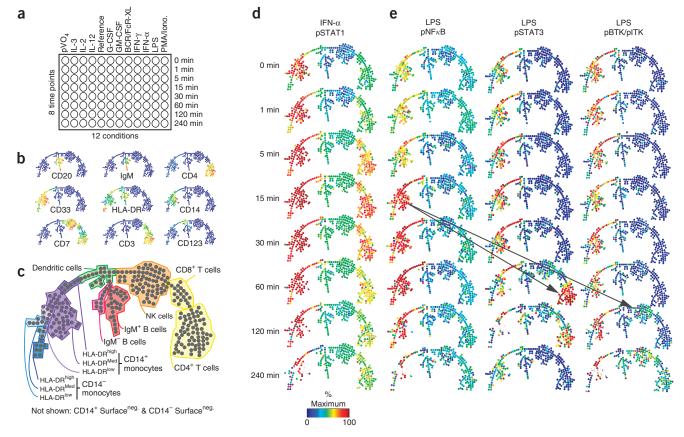
**Figure 2** PBMC signaling time-course experiment. (**a**) Twelve conditions and eight different time points were used to capture time-resolved PBMC signal transduction from 0 to 240 min. (**b**) The expression and localization of cell surface markers within the SPADE tree is shown. (**c**) Fourteen unique PBMC cell types were distinguished by SPADE analysis based on surface marker expression shown in **b**. (**d**) The time-resolved response of the PBMC continuum of subpopulations to IFN-α stimulation by STAT1 phosphorylation, as visualized by SPADE. (**e**) Time-resolved response of the PBMC continuum of subpopulations to LPS stimulation by NFκB, STAT3 and BTK/ITK phosphorylation, as visualized by SPADE. Putative intercellular communication is indicated by black arrows.

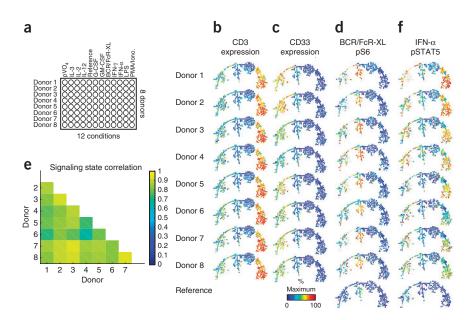progression analysis of density-normalized events (SPADE)[35,36] (**Fig. 2b–e** and **Supplementary Note 2**).

After interferon-alpha (IFN-α) stimulation, STAT1, STAT3 and STAT5 phosphorylation was induced in most cell types[38–40] (**Fig. 2c,d** and **Supplementary Fig. 4**); induction peaked at 15 min and then declined, although elevated STAT1 phosphorylation was maintained for 4 h in B cells and natural killer (NK) cells (**Fig. 2d**). Unlike STAT3 and STAT5, prestimulation and IFN-α–induced phosphorylation levels of STAT1 varied widely among cell types, from a twofold induction in CD14+ monocytes, to a fivefold induction in other cell types (**Fig. 2d**). In IFN-α–stimulated T cells, STAT5 phosphorylation returned to prestimulation levels after initial activation, but time-dependent differences in STAT5 induction were observed in T-cell subtypes (**Supplementary Fig. 5**).

Time-course analysis by MCB also allowed identification of time-dependent phenomena such as feedback regulation (**Supplementary Note 3** and **Supplementary Figs. 6** and **7**) and intercellular communication. Monocytes, which express the lipopolysaccharide (LPS) receptor toll-like receptor 4 (TLR4)[41], responded first to LPS stimulation, with phosphorylation of the canonical LPS pathway members p38, ERK and NFκB peaking at 15–30 min, followed by S6 phosphorylation, which peaked after 2 h (**Fig. 2e** and **Supplementary Fig. 8**), in agreement with previously reported results[42]. Cells with little or no LPS receptor expression[41], including B cells, T cells and NK cells, responded to LPS at later time points. STAT3, STAT5 and ITK

phosphorylation occurred in T cells and NK cells after 2 h and STAT1 phosphorylation in B cells after 4 h (**Fig. 2e** and **Supplementary Fig. 9**), which is likely attributable to intercellular communication through interleukin (IL-6) or other factors, such as TNF-α, which are known to be released by monocytes after LPS stimulation[43]. These results show that the MCB method can be used to identify novel, dynamic signaling events and intercellular communication on the network-scale level in complex, heterogeneous cell samples.

**Comparison of signaling response in PBMCs from multiple donors**
To assess variability in signaling between donors, we interrogated eight PBMC samples using MCB (**Figs. 1** and **3a**). As in the previous experiment, 14 signaling nodes and 10 cell-surface markers were measured over 12 stimulation conditions (**Fig. 3a** and **Supplementary Fig. 6**) and analyzed using SPADE[39]. Samples were collected 30 min after stimulation, as the previous time-course experiment revealed maximal signaling response at this point for most stimulus- and phosphorylation-site pairs.

The percentage of each cell type varied between the donor PBMC samples (**Supplementary Table 1**). Monocytes ranged from 15% (donor 7) to 26% (donor 3), T cells from 29% (donor 3) to 51% (donor 2), and B cells ranged from 5% (donor 2) to 11% (donor 3). A similar range of cell percentages was also visible for the cell subtypes (**Supplementary Table 1**). The relative expression levels of the surface markers used for immune phenotyping were similar across

**Figure 3** Signaling response comparison of PBMCs from eight donors. (**a**) Twelve conditions were used to compare signaling response of PBMCs from eight different donors after 30-min stimulation. (**b**) The expression of the CD3 cell surface marker within the SPADE tree for all donors is shown. (**c**) The expression of the CD33 cell surface markers within the SPADE tree for all donors is shown. (**d**) Comparison of the response to 30 min BCR/FcR-XL stimulation of the PBMC continua of subpopulations of the analyzed donors as visualized by SPADE shown by the median phosphorylation levels of S6 protein. (**e**) Correlation plot of the fold-change induction over all stimuli, phosphorylation site and cell type pairs between donors after 30-min stimulation. (**f**) As **d**, but the median of phosphorylation on STAT5 after 30 min IFN-α stimulation is shown.

the donor samples (e.g., CD3, **Fig. 3b**), except for CD33, with donors 3 and 4 showing lower expression (**Fig. 3c**)[44].

Despite differences in cell type abundances, cell signaling in each cell population was similar across the eight donor samples, including S6 phosphorylation after BCR/FcR-XL induction (**Fig. 3d** and **Supplementary Results 2**). Systematic evaluation of signaling response similarity between donors revealed a high correlation of fold-change induction for each stimulus, phosphorylation site and cell type combination between donors (**Fig. 3e**), ranging from 0.67 (donor 4 versus donor 6) to 0.93 (donor 7 versus donor 8) (**Fig. 3e**). Exceptions existed. Contrary to all other donors, phosphorylation on STAT5 and STAT3 was hardly induced in T cells after INF-α stimulation in donor 6 (**Fig. 3f** and **Supplementary Fig. 10**), but phosphorylation on STAT1 was induced (**Supplementary Fig. 10**), and monocytes of the same donor showed induction of phosphorylation on STAT3 and STAT5 (**Supplementary Fig. 11**). These results show that cellular signaling was largely similar between individual donor PBMC samples, even when the cell type abundances varied.

### Systematic quantification of PBMC response to kinase inhibition
To systematically quantify PBMC response to kinase inhibition, we applied 96-well MCB to PBMCs treated with an eight-step, fourfold dose-response titration of 27 unique small-molecule inhibitors, and used the resulting data to calculate the half-maximal inhibitory concentration ($IC_{50}$) and percent inhibition (**Fig. 4a**). Twelve stimulation conditions were used for 30 min to maximize signaling-space coverage (**Fig. 4b**). Seven channels were used for MCB, 10 for cell-surface marker quantification to resolve 14 cell types (**Fig. 4c**) and 14 to quantify protein phosphorylation sites (**Fig. 4d**), covering important signaling pathways in all cell types for a network-wide signaling map (**Supplementary Fig. 6**). We used a single PBMC donor sample for all inhibitors to allow comparability, and we tested one inhibitor, the JAK1/JAK2 inhibitor ruxolitinib (Jakafi), against four donors to determine inhibitor response variability.

We quantified 18,816 phosphorylation site levels per inhibitor (12 stimuli × 8 doses × 14 cell types × 14 phosphorylation sites), yielding 2,352 dose-response titrations (14 cell types × 14 phosphorylation sites × 12 stimuli) for a total of 63,504 dose titrations. The extracted parameters of all dose response curves, including $IC_{50}$, fold-change, percent inhibition values, the corresponding confidence intervals and Z-prime scores are given in **Supplementary Results 3**. To visualize

the data, we systematically organized the inhibitor $IC_{50}$ values and percent inhibition according by cell type and cell stimulus, and plotted the data in a two-dimensional layout guided by canonical pathways (**Fig. 5** and **Supplementary Results 4–6**).

### Inhibitor selectivity
To assess inhibitor selectivity, we compared the known targets of each inhibitor (**Supplementary Fig. 6**) to its MCB-generated inhibition fingerprint (**Fig. 5** and **Supplementary Results 4–6**). Kinase inhibitors with a wide range of targets based on their *in vitro* inhibition profiles, such as staurosporine[13,14,16,17] (**Fig. 5b,c**, column 22) or the receptor tyrosine kinase (RTK) inhibitor sunitinib (Sutent)[14,16,17] (**Fig. 5b,c**, column 24), reduced phosphorylation levels of at least one measured signaling protein in all cell types under all conditions. In contrast, other inhibitors showed more selectivity for cell type and stimulus.

Next, we analyzed the signaling network response patterns to determine the putative selectivity of inhibitors of the JAK-STAT pathway. Cytokine receptors coupled to the JAK-STAT pathway activate a specific set of JAKs (of the four JAK-family kinases: JAKs 1–3, TYK2) upon ligand binding, which in turn phosphorylate a defined subset of STAT proteins (STAT1–6)[38,39]. Seven of the stimuli used (IFN-α, IFN-γ, G-CSF, GM-CSF, IL-2, IL-3 and IL-12) induce previously reported[38,39] JAK-STAT pairs (**Supplementary Table 2**), allowing the selectivity of JAK inhibitors to be assessed. These inhibitors included ruxolitinib[45], clinically approved for treatment of myelofibrosis; tofacitinib, a JAK3 inhibitor in phase 3 clinical testing against rheumatoid arthritis; lestauritinib, a JAK2 and tyrosine kinase inhibitor entering a phase 1 clinical trial; and several research tool compounds, including JAK2 inhibitor III, JAK3 inhibitor VI and pan-JAK inhibitor I.

We observed reduced phosphorylation of various STATs after inhibition with tofacinib compared to control, when we stimulated diverse cell types with GM-CSF, IL-3, IL-2, G-CSF, IFN-α and IFN-γ, indicating that tofacinib is a pan-JAK inhibitor (**Supplementary Fig. 12a**). Higher $IC_{50}$ values on JAK2-dependent phosphorylation of STAT5 after IL-3 or GM-CSF stimulation compared with JAK1- and/or JAK3-dependent phosphorylation after IL-2 or IFN-α stimulation (**Supplementary Fig. 12a,b**) suggest that both JAK1 and JAK3 and to a lesser extent JAK2 or TYK2 are inhibited by tofacinib. This is in agreement with our *in vitro* kinase inhibition profile (**Supplementary Table 3**), but differs slightly from published *in vitro* data[16].
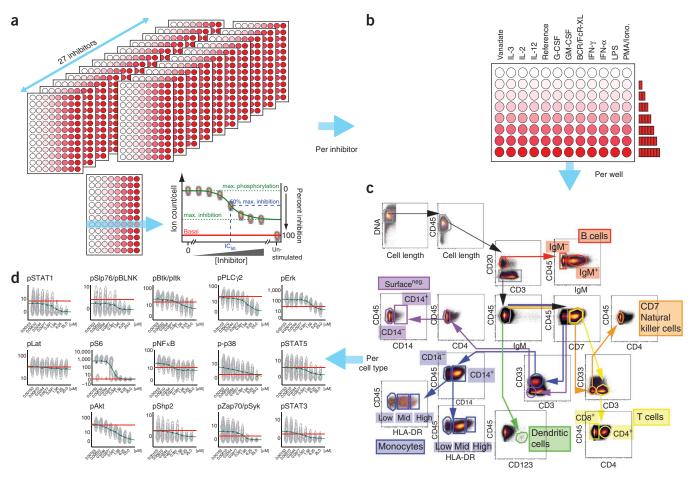
**Figure 4** Analysis of PBMC response to kinase inhibition. (**a**) The effect of 27 inhibitors on PBMC signaling was quantified by MCB, including the IC$_{50}$ value and percent inhibition of phosphorylation levels. (**b**) Experimental set-up for each inhibitor experiment. Twelve stimulation conditions were applied for 30 min in conjunction with an eight-point, fourfold dilution series of each inhibitor. (**c**) Gating scheme. Ten cell surface markers were combined to define 14 cell types. (**d**) For each cell type, 14 phosphorylation sites covering many immune signaling pathways were quantified by mass cytometry. Examples of dose-response curves are shown for staurosporine treatment in CD4$^+$ T cells.

Broad inhibitory effects on STAT phosphorylation after GM-CSF, IL-3, IL-2, G-CSF, IFN-α and IFN-γ stimulation were also observed for ruxolitinib (**Supplementary Fig. 13**), lestauritinib (**Supplementary Fig. 14**) and the pan-JAK inhibitor I (**Supplementary Fig. 15**), in agreement with our *in vitro* inhibition profile (**Supplementary Table 3**). Furthermore, lestauritinib and the pan-JAK inhibitor showed sizeable effects on signaling outside the JAK pathways (**Supplementary Figs. 14** and **15**), indicating that these inhibitors affected many signaling network nodes.

Detailed inhibition profile analysis of JAK2 inhibitor III (**Supplementary Note 4** and **Supplementary Fig. 16a,b**) and JAK3 inhibitor VI (**Supplementary Note 5** and **Supplementary Fig. 17a,b**) indicated inhibition of TYK2 activity by JAK2 inhibitor III and inhibition of JAK1/TYK2 activity by JAK3 inhibitor VI, rather than JAK2 inhibition by JAK2 inhibitor III and Jak1-JAK3 inhibition by JAK3 inhibitor VI (**Supplementary Notes 4,5** and **Supplementary Results 5**). Comparison of the JAK2 inhibitor III MCB results with the *in vitro* kinase assay results were surprising (**Supplementary Table 3**). The JAK2 inhibitor III did not inhibit JAK-family kinases at concentrations ≤10 μM. This discrepancy between *in vitro* and *in vivo* results could be due to an allosteric mechanism of inhibition not recapitulated *in vitro,* or additional off-target effects. The JAK2 inhibitor III structure suggests that it is not an ATP-competitive inhibitor, because

it is bulkier than most ATP-competitive kinase inhibitors and it lacks the critical H-bond donor and acceptor pair[46].

We also analyzed inhibitors of the PI3K-AKT-mTOR-p70S6K signaling pathway (**Supplementary Note 6**, **Fig. 5b** colored boxes and **Supplementary Figs. 18–20**). Taken together, these results show that MCB can be used to generate a cellular inhibitor 'fingerprint' and to investigate target selectivity with unprecedented resolution and throughput in complex cellular mixtures.

## Cell type selectivity
We next investigated the cell type selectivity for each inhibitor by analyzing the signaling response data from 14 cell types. No inhibitor showed exclusive selectivity for a single cell type, and inhibitors with broad pathway activity, such as staurosporine and sunitinib, displayed little to no cell type selectivity (**Fig. 5b,c**, columns 22 and 24). In general, the inhibition profile of HLA-DR$^{mid}$ monocytes differed from those of other cell types (**Supplementary Results 4**). Inhibitors of the Src family kinases (SFKs) and receptor tyrosine kinase (RTKs)—dasatinib, LCK inhibitor and PP2—inhibited SFK downstream signaling components in monocytes compared to other cell types, including SYK, PLCγ2 and BLNK, often independent of stimulation (**Supplementary Figs. 21** and **22**). Many inhibitors in addition to the JAK inhibitors and sunitinib affected JAK-STAT

signaling in monocytes (**Supplementary Figs. 21** and **22**), independent of stimulation conditions, indicating that under the conditions of our assay, SFK and JAK-STAT signaling pathways are active in monocytes, but inactive in T cells, B cells, dendritic cells and NK cells.

The data also enabled the comparative analysis of cell-signaling-network responses to inhibition in closely related cell types. Such responses differ only to a few compounds, including imatinib (Gleevec; **Supplementary Note 7** and **Supplementary Fig. 23**), the c-Jun
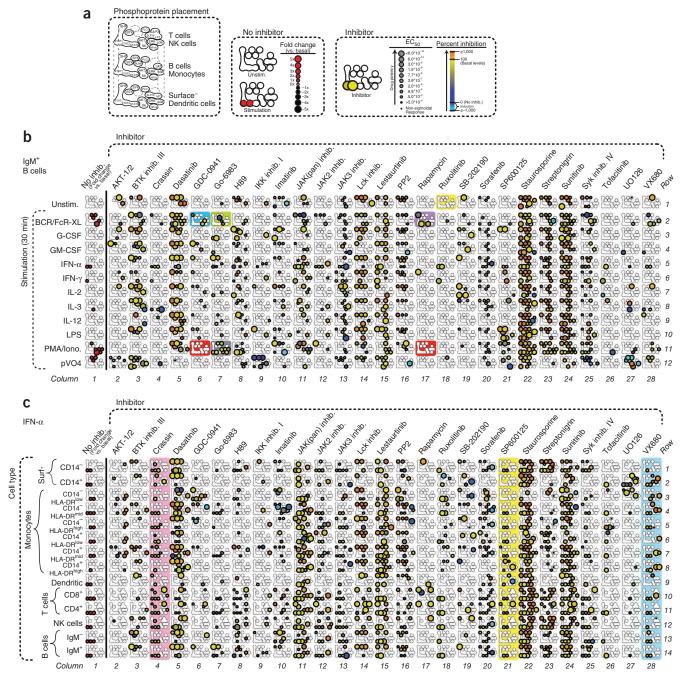
**Figure 5** Overview of inhibitor impact. (**a**) A miniaturized signaling network, guided by canonical pathways, including vertical ordering of nodes from membrane-proximal signaling proteins to nucleus-localized transcription, is used here to depict the effect of a stimulus or inhibitor on each quantified phosphorylation site after 15-min incubation with the inhibitor and subsequent 30-min cell stimulation. As some antibodies recognize different proteins in different cell types, three cell type–specific signaling networks are shown. In the absence of inhibitor ("No inhibitor"), the response to each stimulus relative to the untreated state is represented as fold change by a sized red or black circle (for induction and reduction of phosphorylation levels, respectively). To visualize the effects of inhibitors ("Inhibitor"), circles were sized inversely to the $IC_{50}$ and colored by the percent inhibition ('inhibition'). For example, in the presence of ruxolitinib, inhibition of phosphorylation of STAT1 ($IC_{50}$ = 23 nM, 93% inhibition) and STAT3 ($IC_{50}$ = 4 nM, 147% inhibition) was observed (**a**, "Inhibitor"), whereas without activation of the B cells, no observable effects of ruxolitinib on the quantified signaling nodes were visible (**b**, yellow box). Fold-change induction before inhibition and confidence intervals for $IC_{50}$ values and percent inhibition are not visualized, but are given in **Supplementary Results 3**. (**b**) The impact of all inhibitors under all stimulation conditions is shown for IgM+ B cells. (**c**) The impact of all inhibitors on all cell types after 30 min IFN-α stimulation is shown. Sections highlighted by color are detailed in the main text.
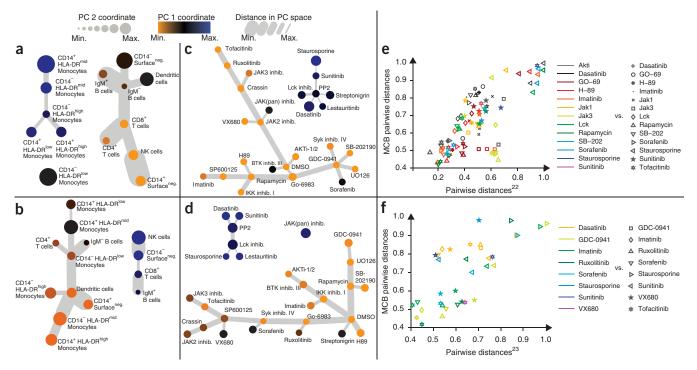
**Figure 6** Principal component analysis of cell type and drug response. (**a**) Cell type PCA across all inhibitors, phosphorylation sites and conditions. (**b**) Cell type PCA for streptonigrin across all phosphorylation sites and conditions. (**c**) Inhibitor PCA across all cell types, phosphorylation sites, and conditions. (**d**) Inhibitor PCA for monocytes after IFN-α stimulation across all phosphorylation sites. (**e**) Pairwise distance correlation plot to show the agreement between *in vivo* data generated by MCB and previously generated[16] *in vitro* kinome inhibition profiles. Distances shown were scaled as a fraction of the maximum distance. (**f**) As **e**, but pairwise distance correlation plot between *in vivo* data generated by MCB and a different set of previously generated[17] *in vitro* kinome inhibition profiles.

N-terminal kinase (JNK) inhibitor SP600125 (**Supplementary Note 7** and **Supplementary Fig. 24**) and the aminoquinone antitumor antibiotic, streptonigrin. Streptonigrin induced differential signaling responses in monocyte subtypes (**Supplementary Note 7** and **Supplementary Fig. 25a–d**) and in T cells and B-cell subtypes on S6, PLCγ2, SLP76/BLNK and STAT5, often independently of the stimulation (**Supplementary Fig. 25c,d**, columns 10–14, yellow boxes). In CD8+ T cells and IgM+ B cells, streptonigrin often had low IC$_{50}$ values and strongly inhibited phosphorylation, but we observed only a weak inhibition in CD4+ T cells and IgM− B cells (**Supplementary Fig. 25c,d**, columns 10–14, yellow boxes) on the same sites. An exception was when cells were stimulated with PMA-ionomycin; inhibition of most signaling molecules was detected in most cell types (**Supplementary Fig. 25d**, row 11, gray and red boxes). Streptonigrin interferes with cell replication, transcription and cell respiration[47], but how this might lead to the observed differences is unclear. An overview of the cell type profiles of each inhibitor tested is shown in **Supplementary Results 4**.

Overall, these results demonstrate that MCB can be used to reveal how different cell types and their underlying signaling network states are uniquely affected by given inhibitors, underscoring the need for deep signaling profiling for supporting the development of cell type-specific compounds.

### Systematic analysis of cell type and inhibitor similarity

We next sought to use the large number of signaling molecules quantified per cell type under many conditions to characterize the cell types and inhibitors. We analyzed the complete data set and the effect of a drug in a single cell type and condition. To analyze cell type similarity, we generated a matrix of IC$_{50}$ values representing the effects of each

inhibitor for each cell type, stimulation and phosphorylation site. Likewise, to analyze inhibitor similarity, we created a matrix of IC$_{50}$ values representing cell type response for each inhibitor, stimulation and phosphorylation site. We performed principal component analysis (PCA) on each of these matrices to ask which cell types or inhibitors were similar in the reduced-dimensionality space.

When the first matrix is used in the PCA to determine cell type similarity, the cell types with related immune functions, such as the lymphocytes, were grouped closely within principal component space, as defined by all determined components (encompassing up to 90% of the total variance), forming their own cluster (**Fig. 6a**). A second and third cluster were formed by the monocyte lineage, with closely related monocyte subtypes being also closest in principal component space. We also carried out biclustering of data for all cell types (**Supplementary Fig. 26**), which showed that at this level of signaling network resolution, the established endpoint topology of hematopoiesis[41] in PBMCs was recapitulated based on signaling network response alone.

When the input matrix was restricted to the streptonigrin-induced signaling responses (**Fig. 6b**), a distinct picture emerged. Closely related immune cell types were differentially affected, as CD8+ T cells, IgM+ B cells, CD14− surfaceneg and NK cells formed their own cluster in principal component space, distant from CD4+ T cells and IgM− B cells. The PCA also captured the differences in inhibitor impact among the monocyte subtypes compared to the PCA over all conditions, in concordance with analysis from the "Cell type selectivity" section (**Supplementary Note 7** and **Supplementary Fig. 25**).

In a second analysis, we transposed the matrix to ask which inhibitors clustered together in the reduced-dimensionality space defined by all cell type signaling states and conditions (**Fig. 6c**). The general kinase inhibitors staurosporine, lestauritinib and streptonigrin and the SFK

and RTK inhibitors sunitinib, PP2, dasatinib and LCK inhibitor formed their own cluster in principal component space, reflecting their overall high impact on signaling networks across cell types and conditions.

By restricting the input matrix to monocytes after IFN-α stimulation across all inhibitors, we addressed the question of which inhibitors similarly affect JAK-STAT signaling (**Fig. 6d**). JAK2 inhibitor III, JAK3 inhibitor VI, tofacinib, crassin, SP600125 (a JNK inhibitor) and VX680 inhibitor formed a tight group. As described above, the JAK inhibitors inhibited JAK-STAT signaling after IFN-α stimulation in most cell types. However, Crassin also displayed a similar profile (**Fig. 5c**, row 4, pink box), reproducing a recent finding[32]. SP600125 was not specific for JNK inhibition, but also inhibited phosphorylation of STAT3 and STAT5 across many cell types (**Fig. 5c**, column 21, yellow box; **Supplementary Fig. 24** and **Supplementary Fig. 27**). The ability of SP600125 to inhibit JAK-STAT signaling was confirmed by *in vitro* kinase inhibition assays (**Supplementary Table 3**). Here IC$_{50}$ values of 974 nM, 736 nM, 344 nM and 440 nM were measured for JAK1, JAK2, JAK3 and TYK2, respectively. VX680, an inhibitor of Aurora kinases, which is also active against BCR-ABL, FLT3 and JAK2 (ref. 48), was close to SP600125 in principal component space. Phosphorylation of STAT3 and STAT5 were inhibited in the presence of VX680 after IFN-α stimulation in many cell types (**Fig. 5c**, column 28, blue box and **Supplementary Fig. 28a,b**, row 5, green box). This suggests that VX680 inhibits JAK1 and, even more potently according to the *in vitro* data, TYK2 (**Supplementary Table 3**). However, for VX680, we observed no or only weak inhibition of phosphorylation on STAT5 after GM-CSF or IL-3 stimulation, indicating the absence of JAK2 inhibition, contrary to the *in vitro* data (**Supplementary Fig. 28b**, red boxes).

These results show that PCA allows characterization and identification of similar cell type responses to a given inhibitor and that the inhibitor-induced signaling states were sometimes independent of cell type and immune function, indicating enormous plasticity in the cellular signaling network. In addition, PCA allowed rapid classification of inhibitors based on their profiles at a given drug exposure or in a given experimental condition, and suggests novel specificities for inhibitors SP600125 and VX680.

### Comparison of inhibition response in PBMCs from multiple donors

To establish whether the inhibition data sets generated from a single PBMC donor are generalizable or if there is variability in inhibitor response between donors, we measured the effects of ruxolitinib on four of the eight donor samples previously described that best represent the variability between donors (**Fig. 3**). The response to inhibition between donors was similar overall, but also showed marked differences (**Supplementary Fig. 29**). Whereas ruxolitinib inhibited INF-α–stimulated phosphorylation on STAT1 on IgM$^+$ B cells, IgM$^-$ B cells and CD4$^+$ T cells in all donors analyzed (**Supplementary Fig. 29**, green boxes), the same site was only inhibited in two out of four donors in CD8$^+$ T cells (**Supplementary Fig. 29**, row 10, red box). Similarly, G-CSF induced phosphorylation on STAT3 in CD14$^-$ HLA-DR$^{mid}$ monocytes was inhibited in all donors except donor 4 (**Supplementary Fig. 29**, row 4, blue box). Closer inspection of these differences in inhibitor response revealed they were often due to inhibition curves that fall directly above or below the $R^2$–fold change cutoff used as a threshold for calling a site 'inhibited' (Online Methods), and this was often compounded by differences in the level of pathway activation observed between donors after stimulation (**Fig. 3**). We have observed such fluctuations in human PBMCs particularly in cases of chronic diseases involving inflammation (G.P.N., data not shown), indicating in part that the

differences observed might indicate differing 'set points' in cell subset–specific activation due to prior immune encounters.

Therefore, we conclude that the 27 state-based kinase inhibitor profiles are a comprehensive resource describing normal healthy immune response to kinase inhibition. These results also underscore the need to measure several donor samples if an inhibitor must be extensively analyzed, for example, before a clinical trial.

### Comparison of *in vivo* versus *in vitro* inhibition profiles

Finally, we examined the agreement between data generated by MCB and previously published *in vitro* kinase assay data, including one study with 14 compounds in common with this study[16], and one study with 9 compounds in common with this study[17] (**Supplementary Results 7**). We compared these data with the matrix of MCB-derived IC$_{50}$ values representing inhibitor impact for each cell type, stimulation and phosphorylation. For the MCB data set and the two *in vitro* data sets, we plotted the pairwise distances between the compounds against each other (**Fig. 6e,f**).

In general, inhibitor relatedness as measured by pairwise distances was similar in the *in vitro* and *in vivo* data sets, resulting in correlation coefficients of 0.74 and 0.75, respectively. An exception was JAK3 inhibitor VI, for which the distance was greater to most inhibitors in the *in vitro* data set compared with the *in vivo* data set. Nevertheless, for most of the compounds analyzed, the *in vitro* inhibition profile (e.g., Go-6983, rapamycin, GDC-0941, JAK inhibitors) is largely in agreement with the MCB data, but caution is necessary because depending upon the stimulation condition, the cell types and the donor samples used for testing, these data may not be generalizable. These *in vivo* and *in vitro* approaches when used together should prove highly complementary for the mechanistic investigation of cellular signaling pathways.

### DISCUSSION

MCB makes possible high-throughput experiments that are impractical to do using FBFC or mass cytometry alone. We used MCB to analyze PBMC signaling dynamics, cell-to-cell communication and to comprehensively profile small-molecule drug regulators based on PBMC signaling network response. In these experiments, 18,816 phosphorylation levels were quantified in 1,344 cell populations from 96 multiplexed samples for each inhibitor. By using $n$ metal isotopes for binary-encoded MCB, $2^n$ samples can be multiplexed. This allows >10,000 samples to be multiplexed in a single tube with 15 channels remaining for antibody detection. At this scale, MCB becomes an attractive technique for high-throughput drug screening and genome-wide RNA interference knockdown studies.

Despite several limitations (**Supplementary Note 8**), the approach presented here allows analyses that span from the systems-level down to single pathways and molecules. In the experiments described, high-level compound classification suggested novel molecular targets and indicated novel mechanisms of action for widely used kinase inhibitors. The ability to identify bio-active compounds such as JAK2 inhibitor III, which presumably would not have been identified by *in vitro* screening, highlights a key advantage to the *in vivo* MCB approach.

As MCB enables signaling events to be monitored over time, it provides an opportunity to study the connectivity of signaling pathways, the effects of inhibitors on feedback signaling[49], and intercellular communication[50]. Time-resolved, single-cell analysis can reveal differences between immediate and subsequent indirect, adaptive effects caused by cross-talk between signaling pathways. Our results indicate that data from *in vivo* MCB and *in vitro* kinome screening methods[16,17] are complementary, suggesting that using both

approaches is a potentially useful paradigm for the investigation of pathway mechanism, connectivity and dynamics.

With high-throughput, systems-level coverage of the most important signaling pathways and their interconnections for each cell type, the cellular signaling states induced by inhibitors could be used as a metric for preclinical development. Similar MCB analyses done on defined disease samples could be used to categorize drug effects or drug combinations, to eventually guide therapeutic strategies based on discrete knowledge of a patient's cellular phenotypes and genotypes. Additionally, the MCB method could be used directly as a tool for personalized medicine, with the pathway activation and drug response of a patient's *in vivo* or *ex vivo* tissue samples used to guide therapy decisions.

## METHODS
Methods and any associated references are available in the online version of the paper.

**Data availability.** All dose response curves can be viewed and all raw data can be downloaded from http://www.cytobank.org/nolanlab/. The determined $IC_{50}$ values, fold changes, percent inhibition values, confidence intervals and Z-prime scores are available in **Supplementary Results 2**.

*Note: Supplementary information is available in the online version of the paper.*

AUTHOR CONTRIBUTIONS
B.B. conceived and designed the experiments, performed all PBMC experiments, MCB multiplexing and mass cytometry analysis, analyzed the data and wrote the manuscript. E.R.Z. conceived and designed the experiments, developed the mDOTA reagents, performed all PBMC experiments, MCB multiplexing and mass cytometry analysis, analyzed the data and wrote the manuscript. R.F. designed and implemented algorithms and software tools for barcode deconvolution, semi-automatic cell-type gating and dose-response analysis. T.J.C. performed PCA and assisted with data analysis. E.S.S. designed and implemented high-density data visualization. R.V.B. designed and implemented scripts for FCS file processing and assisted with SPADE analysis. E.F.S. assisted with SPADE analysis, designed the 96-well barcoding scheme. S.C.B. assisted with antibody labeling and running the mass cytometer, and high-dimensional analysis of human immune cell populations. K.S. helped with bioinformatic data analysis. P.O.K. conceived cell barcoding for mass cytometry. G.P.N. conceived and designed the experiments, wrote the manuscript. All authors read and approved the final manuscript.

COMPETING FINANCIAL INTERESTS
The authors declare competing financial interests: details are available in the online version of the paper.

Published online at http://www.nature.com/doifinder/10.1038/nbt.2317.
Reprints and permissions information is available online at http://www.nature.com/reprints/index.html.

1. Paul, S.M. *et al.* How to improve R&D productivity: the pharmaceutical industry's grand challenge. *Nat. Rev. Drug Discov.* **9**, 203–214 (2010).
2. Nolan, G.P. What's wrong with drug screening today. *Nat. Chem. Biol.* **3**, 187–191 (2007).
3. Kola, I. & Landis, J. Can the pharmaceutical industry reduce attrition rates? *Nat. Rev. Drug Discov.* **3**, 711–715 (2004).
4. Kramer, J.A., Sagartz, J.E. & Morris, D.L. The application of discovery toxicology and pathology towards the design of safer pharmaceutical lead candidates. *Nat. Rev. Drug Discov.* **6**, 636–649 (2007).
5. Kolch, W. & Pitt, A. Functional proteomics to dissect tyrosine kinase signalling pathways in cancer. *Nat. Rev. Cancer* **10**, 618–629 (2010).
6. Bodenmiller, B. *et al.* Phosphoproteomic analysis reveals interconnected system-wide responses to perturbations of kinases and phosphatases in yeast. *Sci. Signal.* **3**, rs4 (2010).
7. Zhang, J., Yang, P.L. & Gray, N.S. Targeting cancer with small molecule kinase inhibitors. *Nat. Rev. Cancer* **9**, 28–39 (2009).
8. Hynes, N.E. & Lane, H.A. ERBB receptors and cancer: the complexity of targeted inhibitors. *Nat. Rev. Cancer* **5**, 341–354 (2005).
9. Irish, J.M., Kotecha, N. & Nolan, G.P. Mapping normal and cancer cell signalling networks: towards single-cell proteomics. *Nat. Rev. Cancer* **6**, 146–155 (2006).
10. Knight, Z.A., Lin, H. & Shokat, K.M. Targeting the cancer kinome through polypharmacology. *Nat. Rev. Cancer* **10**, 130–137 (2010).
11. Arrell, D.K. & Terzic, A. Network systems biology for drug discovery. *Clin. Pharmacol. Ther.* **88**, 120–125 (2010).
12. Irish, J.M. *et al.* Single cell profiling of potentiated phospho-protein networks in cancer cells. *Cell* **118**, 217–228 (2004).
13. Fabian, M.A. *et al.* A small molecule-kinase interaction map for clinical kinase inhibitors. *Nat. Biotechnol.* **23**, 329–336 (2005).
14. Karaman, M.W. *et al.* A quantitative analysis of kinase inhibitor selectivity. *Nat. Biotechnol.* **26**, 127–132 (2008).
15. Bamborough, P., Drewry, D., Harper, G., Smith, G.K. & Schneider, K. Assessment of chemical coverage of kinome space and its implications for kinase drug discovery. *J. Med. Chem.* **51**, 7898–7914 (2008).
16. Anastassiadis, T., Deacon, S.W., Devarajan, K., Ma, H. & Peterson, J.R. Comprehensive assay of kinase catalytic activity reveals features of kinase inhibitor selectivity. *Nat. Biotechnol.* **29**, 1039–1045 (2011).
17. Davis, M.I. *et al.* Comprehensive analysis of kinase inhibitor selectivity. *Nat. Biotechnol.* **29**, 1046–1051 (2011).
18. Melnick, J.S. *et al.* An efficient rapid system for profiling the cellular activities of molecular libraries. *Proc. Natl. Acad. Sci. USA* **103**, 3153–3158 (2006).
19. Evans, W.E. & Relling, M.V. Pharmacogenomics: translating functional genomics into rational therapeutics. *Science* **286**, 487–491 (1999).
20. Kramer, R. & Cohen, D. Functional genomics to new drug targets. *Nat. Rev. Drug Discov.* **3**, 965–972 (2004).
21. Bantscheff, M. *et al.* Quantitative chemical proteomics reveals mechanisms of action of clinical ABL kinase inhibitors. *Nat. Biotechnol.* **25**, 1035–1044 (2007).
22. Bantscheff, M., Scholten, A. & Heck, A.J. Revealing promiscuous drug-target interactions by chemical proteomics. *Drug Discov. Today* **14**, 1021–1029 (2009).
23. Perlman, Z.E. *et al.* Multidimensional drug profiling by automated microscopy. *Science* **306**, 1194–1198 (2004).
24. Singh, D.K. *et al.* Patterns of basal signaling heterogeneity can distinguish cellular populations with different drug sensitivities. *Mol. Syst. Biol.* **6**, 369 (2010).
25. Geva-Zatorsky, N. *et al.* Protein dynamics in drug combinations: a linear superposition of individual-drug responses. *Cell* **140**, 643–651 (2010).
26. Hulett, H.R., Bonner, W.A., Barrett, J. & Herzenberg, L.A. Cell sorting: automated separation of mammalian cells as a function of intracellular fluorescence. *Science* **166**, 747–749 (1969).
27. Perfetto, S.P., Chattopadhyay, P.K. & Roederer, M. Seventeen-colour flow cytometry: unravelling the immune system. *Nat. Rev. Immunol.* **4**, 648–655 (2004).
28. Chattopadhyay, P.K. *et al.* Quantum dot semiconductor nanocrystals for immunophenotyping by polychromatic flow cytometry. *Nat. Med.* **12**, 972–977 (2006).
29. Perez, O.D. & Nolan, G.P. Simultaneous measurement of multiple active kinase states using polychromatic flow cytometry. *Nat. Biotechnol.* **20**, 155–162 (2002).
30. Young, S.M. *et al.* High-throughput screening with HyperCyt flow cytometry to detect small molecule formylpeptide receptor ligands. *J. Biomol. Screen.* **10**, 374–382 (2005).
31. Bartsch, J.W. *et al.* An investigation of liquid carryover and sample residual for a high-throughput flow cytometer sample delivery system. *Anal. Chem.* **76**, 3810–3817 (2004).
32. Krutzik, P.O., Crane, J.M., Clutter, M.R. & Nolan, G.P. High-content single-cell drug screening with phosphospecific flow cytometry. *Nat. Chem. Biol.* **4**, 132–142 (2008).
33. Krutzik, P.O. & Nolan, G.P. Fluorescent cell barcoding in flow cytometry allows high-throughput drug screening and signaling profiling. *Nat. Methods* **3**, 361–368 (2006).
34. Bandura, D.R. *et al.* Mass cytometry: technique for real time single cell multitarget immunoassay based on inductively coupled plasma time-of-flight mass spectrometry. *Anal. Chem.* **81**, 6813–6822 (2009).
35. Bendall, S.C. *et al.* Single-cell mass cytometry of differential immune and drug responses across a human hematopoietic continuum. *Science* **332**, 687–696 (2011).

36. Lou, X. *et al.* Polymer-based elemental tags for sensitive bioassays. *Angew. Chem. Int. Edn. Engl.* **46**, 6111–6114 (2007).

37. Qiu, P. *et al.* Extracting a cellular hierarchy from high-dimensional cytometry data with SPADE. *Nat. Biotechnol.* **29**, 886–891 (2011).

38. Shuai, K. & Liu, B. Regulation of JAK-STAT signalling in the immune system. *Nat. Rev. Immunol.* **3**, 900–911 (2003).

39. Rawlings, J.S., Rosler, K.M. & Harrison, D.A. The JAK/STAT signaling pathway. *J. Cell Sci.* **117**, 1281–1283 (2004).

40. Platanias, L.C. Mechanisms of type-I- and type-II-interferon-mediated signalling. *Nat. Rev. Immunol.* **5**, 375–386 (2005).

41. Novershtern, N. *et al.* Densely interconnected transcriptional circuits control cell states in human hematopoiesis. *Cell* **144**, 296–309 (2011).

42. Akira, S. & Takeda, K. Toll-like receptor signalling. *Nat. Rev. Immunol.* **4**, 499–511 (2004).

43. Andersson, U. & Matsuda, T. Human interleukin 6 and tumor necrosis factor alpha production studied at a single-cell level. *Eur. J. Immunol.* **19**, 1157–1160 (1989).

44. Perez-Oliva, A.B. *et al.* Epitope mapping, expression and post-translational modifications of two isoforms of CD33 (CD33M and CD33m) on lymphoid and myeloid human cells. *Glycobiology* **21**, 757–770 (2011).

45. Deisseroth, A. *et al.* U.s. Food and drug administration approval: ruxolitinib for the treatment of patients with intermediate and high-risk myelofibrosis. *Clin. Cancer Res.* **18**, 3212–3217 (2012).

46. Knight, Z.A. & Shokat, K.M. Features of selective kinase inhibitors. *Chem. Biol.* **12**, 621–637 (2005).

47. Lown, J.W. The mechanism of action of quinone antibiotics. *Mol. Cell. Biochem.* **55**, 17–40 (1983).

48. Pardanani, A. JAK2 inhibitor therapy in myeloproliferative disorders: rationale, preclinical studies and ongoing clinical trials. *Leukemia* **22**, 23–30 (2008).

49. Brandman, O., Ferrell, J.E. Jr, Li, R. & Meyer, T. Interlinked fast and slow positive feedback loops drive reliable cell decisions. *Science* **310**, 496–498 (2005).

50. Jorgensen, C. *et al.* Cell-specific information processing in segregating populations of Eph receptor ephrin-expressing cells. *Science* **326**, 1502–1509 (2009).

## ONLINE METHODS

**Kinase inhibitors.** All inhibitors and the concentrations used are given in the **Supplementary Methods Table 1**.

**Preparation of barcoding reagents.** Two molar equivalents of maleimido-mono-amide-DOTA (Macrocyclics) were added to each metal chloride in 20 mM ammonium acetate, pH 6.0. Solutions were then immediately lyophilized and resulting solids were dissolved in DMSO to 10 mM for long-term storage at −20 °C.

**PBMC isolation, culture and stimulation.** Human peripheral blood, collected based on a protocol approved by an internal review board, was obtained from the Stanford Blood Bank. The samples obtained from healthy donors were collected in heparin sulfate anticoagulant by leukapheresis and stored at room temperature for 4–6 h. PBMCs were isolated by Ficoll-Paque density centrifugation. The isolated PBMCs were resuspended in freezing solution (90% FBS, 10% DMSO) and stored under liquid nitrogen for future use. For each use, PBMCs were thawed and then washed twice with room temperature PBMC media (RPMI, 5% FBS, 2 mM L-glutamine with 100 U/ml penicillin and 100 μg/ml streptomycin), incubated for 1 h at 37 °C in 5% $CO_2$, and then stimulated as shown in the **Supplementary Methods Table 2** by the addition of IL-2, IL-3, IL-12, G-CSF, GM-CSF, interferon-α, interferon-γ or LPS at 30 ng/ml, sodium orthovanadate at 125 μM, phorbol 12-myristate 13-acetate (PMA) at 50 nM, ionomycin at 1 μg/ml, or a mixture of anti-IgG, anti-IgM, anti-IgK and anti-IgL at 10 μg/ml each (BCR/FcR-XL).

**Antibodies used for analyses.** Metal-labeled antibodies were prepared as described[35]. Briefly, antibodies were obtained in carrier protein–free PBS and then prepared using the MaxPAR antibody conjugation kit (DVS Sciences) according to the manufacturer's protocol. After determining the percent yield by measurement of absorbance at 280 nm, the metal-labeled antibodies were diluted in Candor PBS Antibody Stabilization solution (Candor Bioscience GmbH) for long-term storage at 4 °C. Antibodies used in this study are listed in the **Supplementary Methods Table 3**.

**Accuracy and robustness assessment of MCB.** For this analysis K562 cells, a human myelogenous leukemia cell line, either untreated or treated with orthovanadate was used. Orthovanadate is a broadly active protein tyrosine phosphatase inhibitor that increases cellular tyrosine phosphorylation levels. The induction of SH2 domain-containing leukocyte protein of 76 kDa (SLP76) phosphorylation on Tyr696 in the orthovanadate-treated cells was observed to be highly similar in multiplexed samples (**Supplementary Fig. 2**) compared to nonmultiplexed ones, indicating that the MCB method does not alter mass cytometry measurement or introduce artifacts.

**Time-course experiment.** Approximately 20 million PBMCs were aliquoted into a 96-well 2-ml block. After resting for 60 min at 37 °C, the PBMCs were stimulated with agents listed in the **Supplementary Methods Table 2** for 0 min, 1 min, 5 min, 15 min, 30 min, 60 min, 120 min and 240 min.

**Inhibitor dose-response experiments.** Approximately 20 million PBMCs were aliquoted into a 96-well 2-ml block. After resting for 45 min at 37 °C, the PBMCs were pretreated with the indicated small molecule kinase inhibitors for 15 min, and then stimulated with agents listed in the **Supplementary Methods Table 2** for 30 min in the presence of the inhibitor. Small-molecule kinase inhibitors were all dissolved in DMSO before use, and a 1:1,000 concentration of DMSO was used for all conditions, including the uninhibited control wells.

**PBMC fixation and permeabilization.** At the indicated time point after stimulation, 1.6% formaldehyde (final concentration) was added to the PBMC media and cells were incubated at room temperature for 10 min. The formaldehyde was then diluted to 0.8% with additional PBMC media, and the fixed cells were centrifuged at 600g for 5 min at 4°C. After aspirating the supernatant, the cell pellet was resuspended in ice-cold methanol and transferred immediately to −80°C for long-term storage.

**Cell barcoding and antibody staining.** PBMC samples in methanol were brought from −80°C to 4°C on ice, washed once with Cell Staining Media (CSM, PBS with 0.5% BSA, 0.02% $NaN_3$), and then once with PBS. The cells were then resuspended in PBS, and DMSO stocks of the barcoding reagent were added at 1:100 (to 100 nM final concentration). The cells were incubated at room temperature for 30 min, washed three times with CSM, and then pooled into a single FACS tube for staining with metal-labeled antibodies for 1 h at room temperature. A staining volume of 300 μl was used (~$1 \times 10^8$ cells/ml). After antibody staining, the cells were washed twice with CSM, and then incubated for 10 min at room temperature (or overnight at 4 °C) with an iridium-containing intercalator (DVS Sciences) in PBS with 1.6% formaldehyde. The cells were then washed three times with CSM and once with PBS, diluted with water to ~$10^6$ cells per ml, and filtered through a 70-μm membrane just before analysis by mass cytometry.

**Mass cytometry analysis.** Cells were analyzed on a CyTOF mass cytometer (DVS Sciences) at an event rate of ~500 cells per second. The settings of the instrument and the initial post-processing parameters were described previously[34,35]. For each barcoded sample several data files were recorded. These were concatenated using a script developed in house. The cadmium ion signals with the mass over charges of 110, 111, 112 and 114 were summed to create a single representative channel for the CD3-QDot 605 used in the mass cytometry analysis by the Flow Core package (http://www.bioconductor.org/packages/2.3/bioc/html/flowCore.html). Before gating of the cell subpopulations and determination of the $IC_{50}$ values, the data were normalized as described previously[35].

**In vitro kinase assays.** All analyses were performed by Reaction Biology Corporation, Malvern, Pennsylvania, USA, against active JAK1, JAK2, JAK3 and TYK2. The compounds analyzed are shown in **Supplementary Table 3**. All kinase reactions were performed at 10 μM ATP using a 10-step, threefold serial dilution with 10 μM as the highest compound concentration.

**Data analysis.** The cell events measured for the PBMC time-course experiment were analyzed using the software tool SPADE as described in the main text and previously[35,37]. All time-resolved response curves for all cell types and stimuli are shown in **Supplementary Results 1**.

The following summarizes the SPADE algorithm within the context of this time course data set. First, density-dependent down-sampling of all measured cell events to a defined target number with equalization of the representation of rare and abundant cell types was performed. The down-sampled cell events were then clustered based on expression of ten cell surface markers (CD33, CD20, CD3, CD4, CD7, CD123, CD14, CD45, IgM and HLA-DR) into phenotypically similar agglomerates of cells. Those agglomerates of cells phenotypically similar in ten dimensions were connected via edges to draw a minimum spanning tree. Next, an up-sampling step was performed to assign each cell event from the initial data set to the most representative agglomerate. Finally, the minimum spanning tree was projected in two dimensions, and circles of the tree representing cell agglomerates were colored by median intensity level of a given measured parameter allowing visualization of marker expression across the entire cellular hierarchy.

The cell events measured for each inhibitor were gated according to the scheme shown in **Figure 4**. Each cell type was de-barcoded individually to account for differences in the distributions of barcode metals due to differing cell sizes. The de-barcoding was semi-automated for each barcode channel by creating a boundary at the minimum between the two peaks in the density estimate and then trimming 2.5% of the cells on each side of that boundary. Subsequently, each cell was sorted into its barcode well according to the seven-digit binary number assigned. The cells determined to be in the wells stimulated with BCR-XL then had their IgM gates re-drawn because BCR-XL masks the IgM epitope and shifts the IgM distribution to lower signal levels.

The dose-response curves were then computed for every combination of phosphorylation site, modulator and cell type. This was done by fitting the arcsinh-transformed median signal value S at each dose to the sigmoidal functional form $S = \text{Top} + (\text{Bottom} − \text{Top})/(1+10^{\wedge}(\text{hill}^*(\text{LogIC}_{50} − \text{LogDose})))$. The fits were calculated using MATLAB's implementation of a trust region algorithm using a robust bi-square nonlinear least-squares method with each

point weighted by the inverse of the standard error of the mean. To determine which curves showed significant responses, the fitting scheme was first applied to five control plates of cells that were treated with DMSO but not inhibitor. Then the false-positive rate was calculated for varying levels of $R^2$ and fold change cutoffs (**Supplementary Methods Fig. 1a**). An individual curve was considered a responder if it exhibited a combination of $R^2$ and fold change that corresponded to a <1% false-positive rate in the inhibitor-free plates (**Supplementary Methods Fig. 1b**) for a given analyzed phosphorylation site (**Supplementary Methods Fig. 1c**). All dose-response results are shown **Supplementary Results 2–4** or can be viewed at http://www.cytobank.org/nolanlab/ each curve is shown compared to the reference level and is overlaid on individual contour plots for each sample with DNA along their hidden x axes. Empty plots signify samples where there were zero cell counts.

The percent inhibitions reported for all drugs and conditions were those observed at the highest measured inhibitor concentration, regardless of whether saturation of inhibition was observed. For each curve, this was computed by dividing the difference between the fitted curve at zero dose and at the highest inhibitor concentration by the absolute value of the difference between the fitted curve at zero dose and the reference line (**Supplementary Methods Fig. 1**).

**Principal component analysis.** Principal component analysis (PCA) was used to visualize the differences between various groups in the data, including all cell types, as well as the differences between all inhibitors. Features that were used for the PCA consisted of all $IC_{50}$ values. In addition to the overall feature matrix, PCA was run on data stratified by various subconditions, including stimulation conditions. The control replicates were combined and averaged for this analysis. Next, the pairwise Euclidean distance between all pairs of points (cell types or inhibitors) in PCA space was calculated. This distance was calculated including those principal components that recovered 90% of the total variance. K-means clustering was performed using these distances to determine subgroups of data. A best average silhouette value >100 replicates of K-means was used to determine the potential number of clusters for each set of conditions. The final cluster number was determined by inspection of the silhouette plots. To simplify visualization of the overall relationships among data points, a minimum spanning tree was created for each cluster. In order to convey more information, the values of the data points mapped to PCA space are also represented. The color of the node represents each node's location in the first principal component, and the size of the node represents the location of a node in the second principal component. All minimum spanning trees were visualized using Cytoscape. The clustergram in **Supplementary Figure 26** was generated using the same pairwise Euclidean distance matrix described previously.

$IC_{50}$ values contributing the most to principal components of interest were found by determining those values most heavily weighted in each principal component, >2 standard deviations from the mean. All of these methods were run using MATLAB's existing toolkits.

**Data visualization.** All cell density plots and heat maps were created in Cytobank (http://www.cytobank.org/, Cytobank, Inc.).

# Multiplexed mass cytometry profiling of cellular states perturbed by small-molecule regulators

Bernd Bodenmiller, Eli R Zunder, Rachel Finck, Tiffany J Chen, Erica S Savig,
Robert V Bruggner, Erin F Simonds, Sean C Bendall, Karen Sachs, Peter O Krutzik & Garry P Nolan

In the version of this article initially published online, in the legend for Figure 2e, LPS stimulation was said to be by "NFκB, STAT3 and STAT1," instead of by "NFκB, STAT3 and BTK/ITK." The error has been corrected for the print, PDF and HTML versions of this article.